

Fast radio burst detection in the presence of coloured noise

C. F. Zhang^{1,2}, J.W. Xu^{1,2}, Y. P. Men^{3,1,2}, X. H. Deng⁴, Heng Xu^{1,2}, J. C. Jiang^{1,2},
B. J. Wang^{1,2}, K. J. Lee¹★, J. Li⁵, J. P. Yuan⁵, Z. Y. Liu⁵, Y. X. Huang⁶, Y. H. Xu⁶, Z. X. Li⁶,
L. F. Hao⁶, J. T. Luo⁷, S. Dai⁷, R. Luo⁸, Hassan Zakie⁹, Z. Y. Ma⁴

¹Department of Astronomy, Peking University, Beijing 100871, P.R. China

²Kavli Institute for Astronomy and Astrophysics, Peking University, Beijing 100871, P.R. China

³Max-Planck institut für radioastronomie, Auf Dem Hügel, Bonn, 53121, Germany

⁴Bayesian Data Technologies (Wuhan) Co., Ltd., Wuhan, Hubei 430079, China

⁵Xinjiang Astronomical Observatory, National Astronomical Observatories, Chinese Academy of Sciences, Urumqi, Xinjiang 830011, China

⁶Yunnan Astronomical Observatory, Chinese Academy of Sciences, Kunming 650011, China

⁷National Time Service Center (NTSC), Chinese Academy of Sciences, Xi'an City, Shaanxi Province, 710600

⁸CSIRO Astronomy and Space Science, Australia Telescope National Facility, Box 76, Epping, NSW 1710, Australia

⁹Radio Cosmology Laboratory, Department of Physics, Universiti Malaya, Malaysia

Accepted 2021 March 16. Received 2021 March 16; in original form 2021 January 27

ABSTRACT

In this paper, we investigate the impact of correlated noise on fast radio burst (FRB) searching. We found that 1) the correlated noise significantly increases the false alarm probability; 2) the signal-to-noise ratios (S/N) of the false positives become higher; 3) the correlated noise also affects the pulse width distribution of false positives, and there will be more false positives with wider pulse width. We use 55-hour observation for M82 galaxy carried out at Nanshan 26m radio telescope to demonstrate the application of the correlated noise modelling. The number of candidates and parameter distribution of the false positives can be reproduced with the modelling of correlated noise. We will also discuss a low S/N candidate detected in the observation, for which we demonstrate the method to evaluate the false alarm probability in the presence of correlated noise. Possible origins of the candidate are discussed, where two possible pictures, an M82-harbored giant pulse and a cosmological FRB, are both compatible with the observation.

Key words: methods: data analysis – radio continuum: transients

1 INTRODUCTION

Fast radio bursts (FRBs) are bright (50 mJy–100 Jy) millisecond-duration bursts observed in radio frequency as initially noticed by Lorimer et al. (2007). The FRB signals, propagating through ionised medium, usually show frequency-dependent dispersion features following the cold-plasma dispersion relation, i.e. the pulses in high frequency band arrive earlier than those in low frequency. The time delay between high and low frequency (ν_{high} and ν_{low}) is $\Delta t = 4.15 \text{ ms} \times \text{DM}(\nu_{\text{low, GHz}}^{-2} - \nu_{\text{high, GHz}}^{-2})$, where DM is the electron column density along the line of sight in the unit of $\text{cm}^{-3} \text{ pc}$. The observed DM values of FRBs usually exceed those allowed by the Milky Way, which indicates the FRB sources are at extragalactic or cosmological distances. About 120 FRBs had been detected (Petroff et al. 2016)¹, and more than 20 of them reported to repeat (Spitler et al. 2016; CHIME/FRB Collaboration et al. 2019a,b; Kumar et al. 2019; Luo et al. 2020a). Recently, the origin of an FRB

had been successfully traced to the magnetosphere of a magnetar (Luo et al. 2020c; CHIME/FRB Collaboration et al. 2020; Bochenek et al. 2020), yet the burst trigger mechanism is still unknown (Lin et al. 2020).

FRBs have significant astrophysical applications, which cover a wide range of topics, e.g. testing the Einstein's equivalence principle (Wei et al. 2015; Tingay & Kaplan 2016; Zhang 2016), constraining the rest mass of photons (Wu et al. 2016; Bonetti et al. 2016, 2017; Shao & Zhang 2017), revealing hidden baryons in the Universe (McQuinn 2014; Macquart et al. 2020), studying the dark-energy equation of states (Zhou et al. 2014), probing the cosmological matter distribution (Masui & Sigurdson 2015).

Finding a larger sample of FRBs is the key to understand the FRB burst trigger mechanism and to probe the astrophysics. The FRB searching is thus one of the most important observational activities in the field. Although FRBs are bright bursts, their short durations limit the signal-to-noise ratio (S/N). In order to detect FRBs, most of the FRB searching algorithms are to optimize the FRB detection in the presence of radiometer noise (Cordes & McLaughlin 2003; Men et al. 2019). The matched filter being used in those in-

★ E-mail: kjlee@pku.edu.cn

¹ FRBCAT: <http://www.frbcat.org>

vestigations is the *most powerful statistics* for detecting burst signals with the predetermined waveforms (Vainshtein & Zúbakov 1970). It is *asymptotically optimal* (Van der Vaart 2000), i.e., it archives the best possible detection ability, when the signal-to-noise ratio is large. Indeed, several FRB searching softwares use box-car matched filter as the burst signal detectors, e.g. HEIMDALL² and BEAR (Men et al. 2019). Two major key assumptions of the matched filter approach in signal detection are, 1) the waveform of the signal to be detected is known and 2) the statistical properties of the noise are known. The performance of the detector thus depends closely on the noise model.

One of the major obstacles in FRB searching is the interference in radio band. The radio frequency interferences (RFIs) can mimic the FRB features in terms of the intensity, pulse width and dispersion feature (Burke-Spolaor et al. 2011). Men et al. (2019) had detected an RFI which resembles the FRB signal very well. Significant efforts had been applied to reduce the impact of RFIs on FRB searching. For example, methods such as RFI mitigation and machine learning in FRB candidate sifting, had both reduced the number of false positive detections (Zhang et al. 2018; Agarwal et al. 2020; Zhang et al. 2020). For strong RFIs, one usually mitigates the effects by subtracting them from data. Weak RFIs, on the other hand, are hard to be subtracted. Hence, the correlated noise (or coloured noise) will be left in the data.

The correlated noise is well known in radio astronomy, and it may emerge from many different processes, e.g., flicker noises (Press 1978), propagation effects (Gwinn & Johnson 2011), signal-chain gain instability (Gallego et al. 2004), and low level RFIs (Dewey 1994). Investigating the origin of the correlated noise in FRB searching data is beyond the scope of this paper. Here we focus on the impact of the correlated noise on FRB searching.

We will show in Section 2 that the correlated noise increases the false alarm probability for FRB detection dramatically, and the distribution function of the burst parameters will also be affected. We will investigate the S/N and pulse width distribution of the false positives. We use real observational data to illustrate the application of the correlated noise modelling in Section 3, where we also discuss the evaluation of false alarm probability for single event, where a potential FRB candidate found during the observation of the M82 galaxy is used as an example. Discussions and conclusions are made in Section 4.

2 DETECTION STATISTICS

One can show (Men et al. 2019) that the optimal statistic S , in the sense of the *asymptotically most powerful test* (Van der Vaart 2000), for detecting the pulse signal of square waveform from the background of uncorrelated Gaussian noise is

$$S = \frac{1}{N_{\text{box}} \sigma^2} \left(\sum_{|t-t_0| < w} s_i \right)^2, \quad (1)$$

where N_{box} is the number of data points within the time span of the burst, specified by pulse width w , pulse epoch t_0 , and time t with $|t - t_0| < w$, σ is the root-mean-square level of the Gaussian noise. With such a statistic, one will claim that a burst is detected, if the statistic S is greater than a pre-set threshold S_0 . The null

distribution of S , i.e. the distribution of S when the data contains only noise but no bursts, follows the one degree of freedom χ^2 distribution (Cordes & McLaughlin 2003; Men et al. 2019). The false alarm probability, i.e. the probability of reporting a ‘detection’ due to statistical fluctuation when no real burst happens, becomes

$$P_f(S \geq S_0) = \text{erfc}(\sqrt{S_0/2}). \quad (2)$$

Here, function erfc is the complementary error function. This statistic is constructed under a rather ideal condition, where only the uncorrelated Gaussian noise is assumed. When we include coloured noise, i.e. noise with temporal correlation, the statistical distribution of S differs from the above result. As shown in Appendix A, the detection statistic S follows the ‘scaled’ one degree of freedom χ^2 distribution. Both the mean and standard deviation of statistic S increase. The revised false alarm probability affected by the correlated noise becomes

$$P'_f(S \geq S_0|\eta) = \text{erfc}(\sqrt{S_0/2\eta}). \quad (3)$$

We find that the scale factor η can be approximated by

$$\eta = 1 + N_{\text{box}} \kappa \frac{\sigma_r^2}{\sigma^2 + \sigma_r^2}, \quad (4)$$

with κ being a numeric factor depending on the noise spectral shape and σ_r being the root-mean-square (RMS) level of the coloured noise. For power-law noise, as explained in Appendix A, $\kappa \simeq 1/100$.

The relation between white-noise-only false alarm probability P_f and the one including the coloured noise component is plotted in Figure 1. One can see that the false alarm probability computed using the equation (2) will be underestimated, if the signal contains coloured noise. The larger η is, the more one will underestimate the false alarm probability. That is, a high value of S may come from correlated noise contribution rather than from real burst signals.

As shown in equation (4), two factors play the roles, 1) the amplitude of the coloured noise (σ_r) and 2) the number of data points (N_{box}) within the given pulse. One can see that a higher RMS level of coloured noise or a wider pulse introduces a larger bias on the false alarm probability computation. N_{box} in equation (4) reflects the fact that a wider pulse (corresponding to a lower frequency in frequency-domain spectrum) contains more coloured noise contributions. For a typical case, the data sampling time scale is about 100 μs and the FRB signal lasts for a few milliseconds, $N_{\text{box}} \sim 10 - 10^2$. Considering $\kappa \simeq 0.01$, the red noise component plays a significant role, when its RMS level is compatible with the white noise.

The correlated noise also changes the *finite-sample false alarm probability*, which is defined as the false alarm probability for all candidates with all possible parameter combinations. With coloured noise, the false alarm probability of a single event depends on η . The finite-sample false alarm probability ($P(S \geq S_0)$) is found by integrating over all possible value of η , i.e.

$$P_f(S \geq s_0) = \int P'_f(s \geq s_0|\eta) f_\eta(\eta) d\eta \quad (5)$$

where f_η is the probability density of η . We have $f_\eta \propto T/N_{\text{box}}$, if the data length is fixed to be T .

3 A REPRESENTATIVE EXAMPLE

3.1 Observation and data reduction

We now show the application of the above theory. The data for the demonstration was taken with Nanshan 26-meter (NS26m) radio telescope, which was observing the M82 galaxy at that time.

² developed by Andrew Jameson and Ben Barsdell, <https://sourceforge.net/p/heimdall-astro>

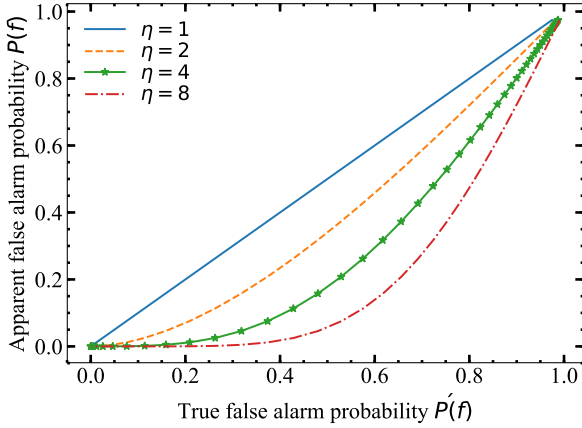


Figure 1. The relation between the true false alarm probability P_f' (equation (3)) and the apparent false alarm probability P_f (equation (2)). The scale factor η is labelled in the figure.

Table 1. Setups at NS26m, KM40m and HRT for M82 observation

Telescope	BW MHz	f_{central}^1 MHz	f_{ch}^2 MHz	Gain K Jy^{-1}	T_{sys}^3 K	Δt^4 μs
NS26m	320	1560	0.97	0.1	25	65
KM40m	440	6690	0.2	0.2	96	65
HRT	800	1400	0.097	0.2	100	163

¹ Central frequency of observation

² Channel width

³ System temperature

⁴ Time resolution

The NS26m is operated by Xinjiang Astronomical Observatory (XAO) of Chinese Academy of Science. Its location is N43°28.27', E87°10.67' with the altitude of 2080m (Wang et al. 2001). We perform observations centred at 1560 MHz with bandwidth of 320 MHz, i.e. from 1.4 GHz to 1.72 GHz. NS26m has a cryogenic front-end and the total system temperature is 25 K. The radio frequency signal is down converted to intermediate frequency of 100–420 MHz with a local oscillator at 1300 MHz.

We also used data collected from the Kunming 40-metre (KM40m) and the Haoping 40-metre (HRT) radio telescopes. KM40m is operated by Yunnan Astronomical Observatory Chinese Academy of Sciences. It locates at N25°02', E102°47' with the altitude of 1985 m (Hao et al. 2010). We use C-band (6.7 GHz) data of KM40. The HRT at Haoping (N34°, 10.5' E109°56.97') (Luo et al. 2020b), is operated by National Time Service Center, Chinese Academy of Sciences. The electronic specification and observation configuration of the telescopes are given in Table 1.

We use the RECONFIGURABLE OPEN ARCHITECTURE COMPUTING HARDWARE ^{2,3} based system to digitize the signal at NS26m, where we form 1024 channels using polyphase filter and integrate the intensity to form filterbank data with 65 μs sampling time. The filterbank data packets are then transferred to a data recording computer using 10 Gigabit Ethernet.

We observed M82 with NS26m for five times from 2016 to 2017. The total observing time is 55 hours. The FRB searching is performed in realtime using the software package BURST EMIS-

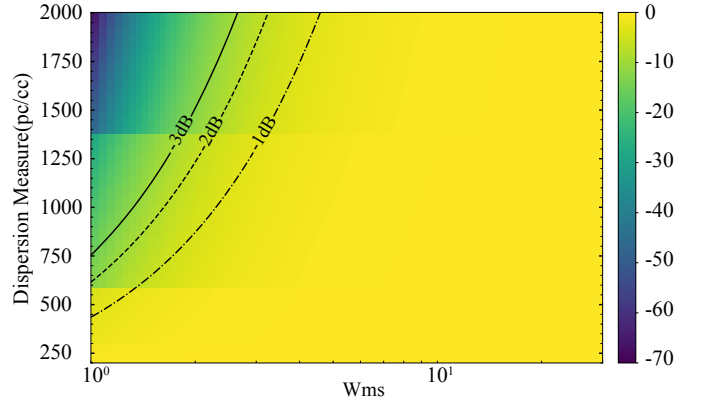


Figure 2. The S/N loss curve caused by sub-band incoherent de-dispersion process. Here our computation uses NS26m parameters. The S/N loss includes effects of inter-channel DM smearing, searching DM step size, and downsampling. X-axis is the pulse width in ms, and Y-axis is the DM of the source. The S/N loss is given in dB, i.e. $10 \log_{10} (S/N)$. The contour lines represent the total S/N loss for 1, 2 and 3 dB.

SION AUTOMATIC ROGER (BEAR, Men et al. 2019). In BEAR, radio frequency interference (RFI) mitigation, de-dispersion, box-car matched filter pulse detection, and candidate clustering are performed. There are two RFI mitigation steps in our pipeline: we first remove data of the channels around 1.55 GHz, because of the RFI induced by satellite communication, and then we use the zero-DM matched RFI filter (Men et al. 2019) to remove wideband interference without dispersion features. We further neglect all candidates with DM below $200 \text{ cm}^{-3} \text{ pc}$ in our analysis to remove the zero-DM RFI contamination.

The data was downsampled before de-dispersion to reduce the computational cost. The parameter of downsampling is tuned together with the DM steps in de-dispersion. We choose the largest possible DM step such that the pulse smearing induced by DM-mismatching is less than the inter-channel DM smearing. The downsampling time resolution is chosen such that it is also smaller than the inter-channel DM smearing. In this way, we minimize the computational cost without downgrading the minimal width of detectable pulses, and the smearing effects are mainly affected by the inter-channel DM smearing.

Subband de-dispersion was used in BEAR to speed up the computation, where we divided the filterbank data into subbands and de-dispersed the data into a coarse grid of trial DMs. The de-dispersed subband data are then further de-dispersed to the required fine DM grids (Men et al. 2019). We chose DM range from 200 to $2000 \text{ cm}^{-3} \text{ pc}$. Our plan of de-dispersion is listed in Table 2. The calculation of the S/N loss is shown in Figure 2, where one can see that our setup is sensitive to FRBs with widths larger than 3 ms for $\text{DM} < 2000 \text{ cm}^{-3} \text{ pc}$.

After the candidate plots are generated, the plots are visually inspected to see if there is a wideband burst signal with a dispersive signature. There are about 1.4×10^4 candidates generated with $S/N \geq 7$. The multi-dimensional distributions for the candidate parameters S/N, width, and DM are shown in Figure 3. Four notable features in Figure 3 are topic-related for the discussion later in the paper, 1). the candidate number is much larger than expected; 2). the candidate S/N distribution shows long-tailed feature; 3). candidate counts correlate with the pulse width; 4). S/N correlates with the pulse width.

³ ROACH2: <https://casper.ssl.berkeley.edu/wiki/ROACH2>

Table 2. The de-dispersion plan for data of NS26m.

DM range (cm^{-3}pc)	ΔDM^1 (cm^{-3}pc)	Downsampling ratio	ΔsubDM (cm^{-3}pc)	Subband number	τ_{ch}^3 (ms)	$\tau_{\Delta\text{DM}}^4$ (ms)
200.0 - 300.5	0.5	4:1	8	12	0.3	0.4
300.5 - 591.5	1.00	8:1	17	17	0.6	0.7
591.5 - 1389.5	3.00	16:1	18	45	1.2	2.0
1389.5 - 2004.5	5.00	32:1	18	34	2.0	3.0

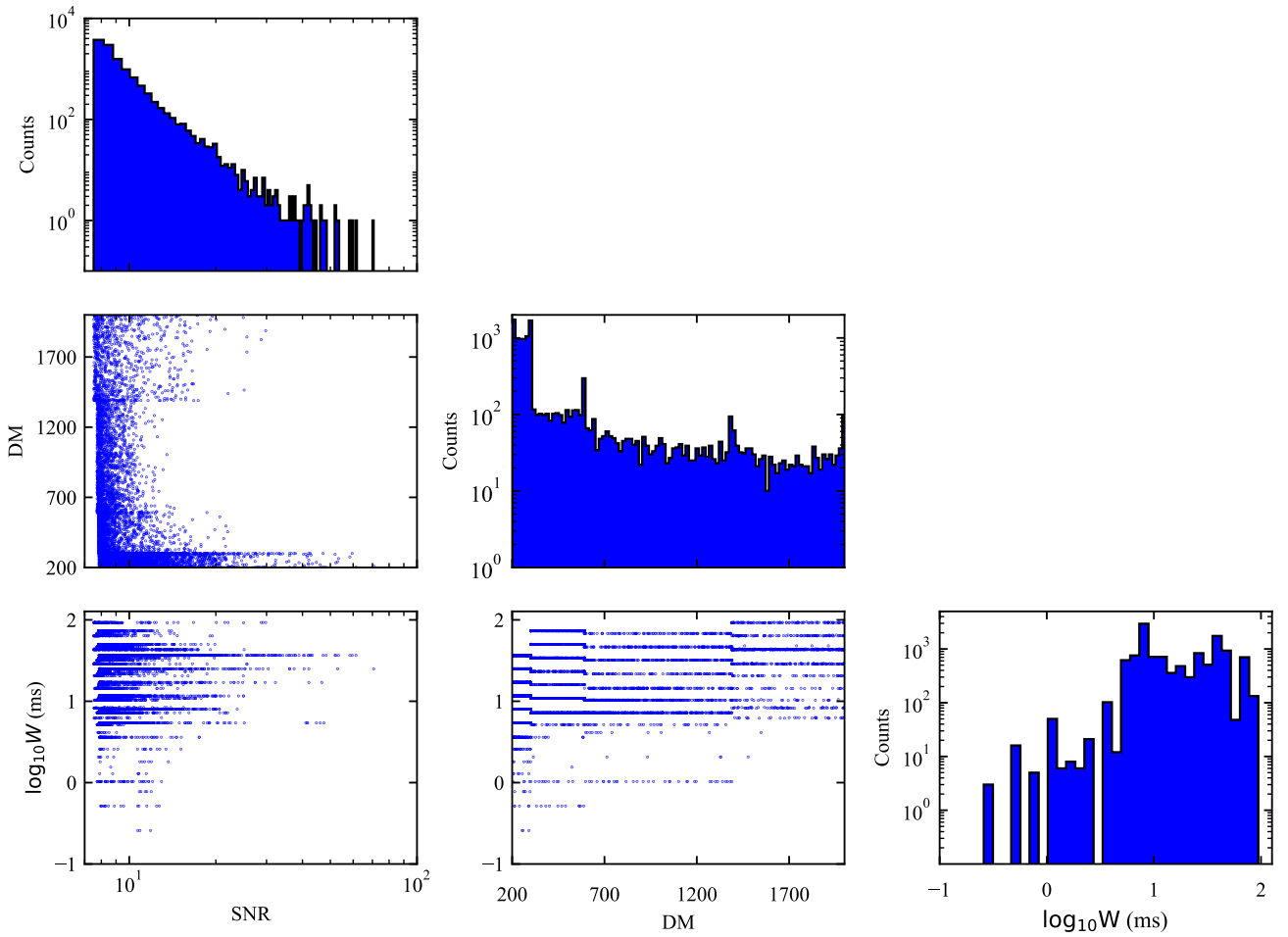
¹ DM step size² Subband DM step size³ Maximal inter-channel DM smearing time scale⁴ DM-mismatch smearing time scale

Figure 3. Candidate distribution of NS26m for DM, pulse width W_{ms} and S/N. Here we only include the candidates with $\text{S/N} \geq 7$. The diagonal histograms are one-dimensional distributions for each parameter, i.e. S/N, DM, and logarithmic pulse width. The off-diagonal scatter plots are for the two-dimensional distributions of parameter pairs. A few peaks in DM distribution, i.e. around $\text{DM} \approx 300, 600$, and 1400 , are due to our de-dispersion plan as shown in Table 2. On the boundaries of the de-dispersion plan, bursts were searched ‘twice’, as the de-dispersion plan segmentation overlaps. Furthermore, if the true DM of a burst is slightly outside the de-dispersion range, the searched DM value is forced to be on the boundary. In this way, high S/N candidates further pile up on the DM boundaries.

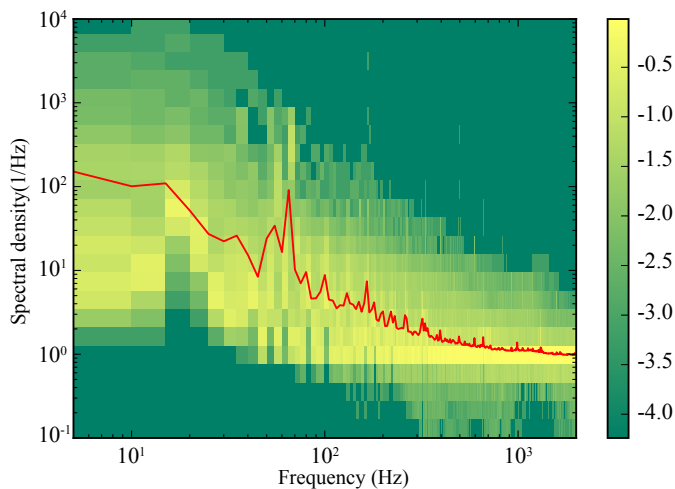


Figure 4. The noise spectrum of 0-DM time series. The x-axis is the frequency in Hz, and the y-axis is the spectral density estimated using Hamming windowed Fourier transform. The red solid curve is the average of all spectra. The background colour scale is the 10-based logarithmic probability of occurrence for the noise power as the given frequency and spectral density. The colour bar on the right side indicates the probability.

Those four features are unexpected in white Gaussian noise modelling (Cordes & McLaughlin 2003; Men et al. 2019). To understand the four features, we need to characterise the correlated noise. We measured the correlated noise spectrum by performing windowed spectral analysis on zero-DM one-dimensional time series. The data was divided into a number of one-second segments, and the Hamming windowed Fourier transform (Harris 1978) was applied to estimate the spectral density. The spectral density of all the data is collected in Figure 4. As one can see that the average spectrum is *dominated* by low-frequency correlated noise, and the spectral density drops as the frequency increases, only at frequency above a few kHz, the spectral density curve gradually turns flat. Obviously, the false alarm probability will be underestimated, if we use the white-noise-only model.

The intensity and shape of red noise spectrum fluctuate time-to-time, as indicated by the background colour shade in Figure 4. The data can be ‘white’ or ‘red’ for a short duration. Since, by *average*, the red noise dominates the noise spectrum, we have $\eta \approx 1 + N_{\text{box}}\kappa \sim 1 + 0.01N_{\text{box}}$.

We can check the distribution of all-candidate S/N as shown in Figure 5. The distribution of detected candidates deviates from the χ^2 distribution. Because the expected S is higher for pulses with larger width. The wider pulses will induce a higher S/N distribution tail. The measured distribution indeed has a tail extending to higher S/N. The false alarm probability will be underestimated, if one assumes χ^2 distribution, i.e. equation (2). The correct version of false alarm probability can be computed by including the correlated noise modelling, i.e. by using equation (5). As one can see in Figure 5, equation (5) produces S/N distribution similar to what see in the data.

We can further see that the false alarm probability calculated using equation (2) does not agree with the number of candidates. If only white noise is assumed, $S/N \geq 7$ is equivalent to $S \geq 49$, and one gets the false alarm probability of $P_f \approx 2.6 \times 10^{-12}$ according to equation (2). It is contradicting that we detected approximately 1.4×10^4 candidates for 55

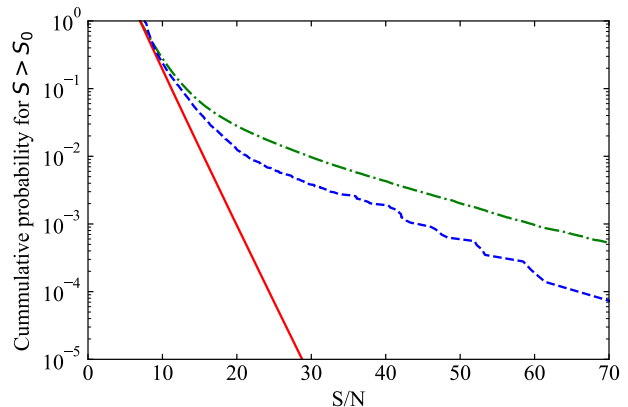


Figure 5. The relation between S/N and cumulative probability for candidates with $S \geq S_0$. The x-axis is the S/N, i.e. \sqrt{S} , and the y-axis is the cumulative probability for $S \geq S_0$. The measured cumulative distribution is plotted in blue dashed curve. The red solid curve is computed from the χ^2 distribution, i.e. equation (2). The green dash-dotted curve are computed from equation (5), which includes the correlated noise contribution.

hours observation, where the expectation detection number is about $N \approx 2 \times 10^{-4}(P_f/10^{-12})(T/55\text{h})(w/\text{ms})^{-1}$. If we include the coloured noise modelling, the expected number of candidates N_c is

$$N_c = \sum_{w_i} P_f(S \geq 7|\eta(w_i)) \frac{T}{w_i}, \quad (6)$$

where the summation is performed over all pulse width w_i used in the pulse searching. The above equation gives $N_c \approx 1.5 \times 10^4$, which matches what we see in real data.

We also note that the pulse width is correlated with the detection statistic S , which reflects the coloured noise effect. As shown in Figure 6, there seems to be an increase of S/N with larger pulse width. For pure white noise modelling, the correlation is not expected. After including the coloured noise, i.e. equation (5), we can understand such a correlation.

3.2 An interesting candidate

For 55 hour data, all candidates with $S/N \geq 5$ were visually inspected. Particularly, volunteers had helped to perform the visual inspection of all candidates more than once. We organised the visual inspection campaign by collaborating with *Bayesian Data Technologies (Wuhan) Co., Ltd* (BDT). BDT helped to remove the axes of candidate figures, and embedded the candidate plots into their mobile game *Lighthouse Project*, aiming at popularizing science⁴. The players of the game are encouraged to acquire more credits by identifying the contents of figures. In the game, the players need to first pass a training session. In the session, examples of known FRB signals were shown to the players together with explanation of the contents. Common concepts in astronomy are introduced, e.g. dispersion, frequency, and intensity. In this way, the players can understand what were shown to them. After the training, candidate plots were shown, and the players started to help identify the FRB signals. Each candidate plot was passed to several players, and

⁴ <http://www.bayesiandt.com/>

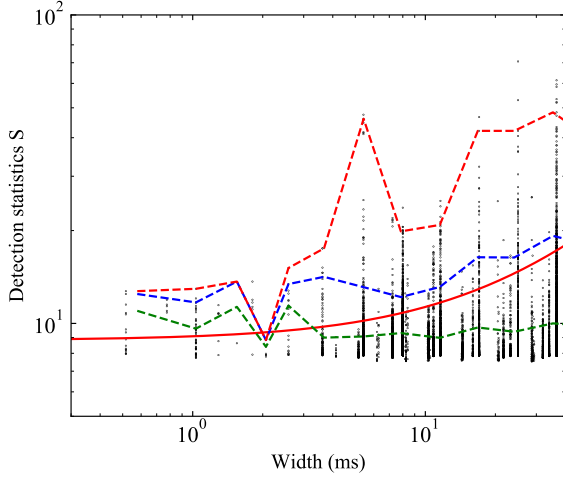


Figure 6. The relation between pulse width (x-axis) and detection statistic (y-axis). The black dots are for all candidates found in observation. The solid line in green shows the average value of the detection statistic as a function of pulse width, while the solid blue and red curve are the 95% and 99.7% envelope. The corresponding curves in dash lines are the same curve computed from red noise modelling, i.e. from equation (5).

BDT helped to identify the common votes from players. We also tested whether there are candidates being missed by the volunteers. This is done by showing known FRB signals to the players, and the ‘performance’ of each player can be evaluated by computing the probability of missing true FRBs.

With the help of volunteers, we also looked at those weaker bursts with $5 \leq S/N \leq 7$. We found one interesting candidate within the entire 55 hour NS26m observation. The pulse profile, de-dispersed dynamical spectra, and S/N-DM-t diagnosis plot of the candidate is shown in Figure 7. More details can be found in Appendix B. The candidate exhibits wideband emission, ‘-2’-index DM signature, but with low S/N. Those properties make it hard to investigate the origin of the candidate. It can be either a RFI or a real FRB. We estimated the flux and fluence of the burst to be 0.6 Jy and 7 Jy ms, using the gain (0.1K/Jy), system temperature (25 K) of NS26m, and effective bandwidth of 280 MHz after RFI mitigation.

The pulse may come from statistical fluctuations. The S/N of the pulse is 6.0, which corresponds to $S = 36$ and $P_f \approx 2 \times 10^{-9}$ for pure white noise case. Given the pulse width of 9 ms and total 55 hour observation time, there will be 2.2×10^7 independent 9-ms segmentations. Thus, if only the white noise is considered, one will expect the chance to find such a ‘burst’ due to the *accidental* statistical fluctuation is about 1%. As we have shown in the previous section, red noise would increase the apparent S and significantly increase the false alarm probability. Could the candidate be caused by the red noise then? We extracted eight-second data around the burst, and measured the noise power spectrum of zero-DM time series. The spectral density is plotted in Figure 8. We estimate the white noise contribution by fitting a horizontal line for frequency above 100 Hz. We then measured the red noise contribution, by subtracting the white noise component from the total spectrum. For the 8-second data around the pulse, the red noise component contribution is only about 6% of total power, i.e. $\sigma_r^2 / (\sigma^2 + \sigma_r^2) \approx 6\%$. The data around this pulse seems to be less affected by red noise. According to equation (4), red noise is incapable of affecting

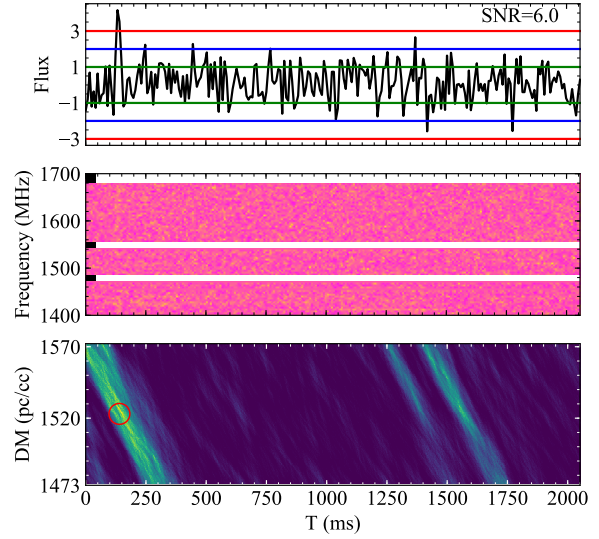


Figure 7. Dynamical spectra of a weak burst ($S/N \approx 6$, after RFI zapped) detected with NS26m telescope (320MHz). Top: normalised pulse profile. The pulse width is approximately 9 ms. Middle: dynamical spectrum of the pulse. The pulse has been de-dispersed to DM 1522.8 pc cm³ to get maximal $S/N = 6$. We reduce the number of frequency channel to 82 (channel width of 3.9 MHz) and time resolution to 1.15 ms, the total effective bandwidth is 280 MHz. After de-dispersing with cold-plasma dispersion relation, i.e. f^{-2} -law, the signal in each channel are aligned in time. Bottom: S/N as a function of time and DM trials. The red circle indicates the pulse position in DM-time parameter space.

the S estimation significantly. We should be able to trust the $6\text{-}\sigma$ S/N and 1% false alarm probability for 55-hour observation. From probability point of view, it is preferred that the burst is real and not from statistical fluctuation.

Follow-up observations for the source were carried out using KM40m and HRT. We observed 12 hours with KM40m on 8th Nov. 2019 using 6.7 GHz center frequency, and 12 hours with HRT on 30th Dec. 2019 at 1.4 GHz center frequency. Unfortunately, neither HRT nor KM40m detected any convincing pulse in the DM range from 1520 to 1526 cm⁻³ pc with $S/N \geq 6$, and the flux limits are ≤ 1.4 Jy (1.4GHz) and 0.7 Jy (6.7GHz) respectively, assuming the pulse width of 9 ms as measured by NS26m.

4 DISCUSSION AND CONCLUSION

In this paper, we investigate the effects of correlated noise in the false alarm probability computation for FRB detection problem. In the presence of correlated noise, particularly red noise, the false alarm probability becomes larger than the case where only white noise is included. The correlated noise also introduces a dependence of false alarm probability on the pulse width. Particularly, for the red noise case, one will detect more candidates with larger pulse width. We have also used observation carried out at NS26m radio telescope to show the application of the false alarm probability computation. We can reproduce the expected number of candidates and their statistical properties. We also show one interesting candidate found in M82 observation.

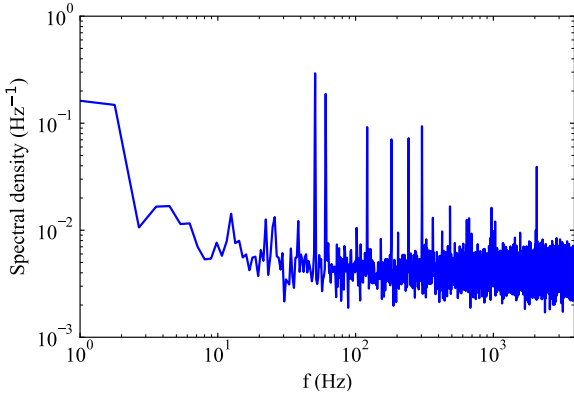


Figure 8. The noise spectrum of the data shown in Figure 7. The x-axis is the frequency, and the y-axis is the power spectrum density. Besides the white noise components (horizontal part with frequency higher than 100 Hz), there is a low frequency red noise components together with several periodic components, which may come from RFIs. By subtracting the white noise component, we measured that the ratio between red noise power and total noise power is $\sigma_r^2 / (\sigma_r^2 + \sigma_w^2) \approx 6\%$, with sampling time of 130 μs .

The burst appears in the direction of M82, however we can not directly associate the burst with M82. The beam size (in solid angle) of NS26m is roughly 16 times of the angular size of M82 (approximately $11.6' \times 3.7'$ (Jarrett et al. 2003)). In fact, NASA/IPAC Extragalactic Databases⁵ show that there are 1458 known galaxies in the NS26m field of view. If we assume the source resides in M82, given the luminosity distance of 3.6 Mpc for M82, the isotropic peak luminosity of the burst will be $L_{\text{iso}} \sim 3 \times 10^{36} \text{ erg/s}$, which will be four orders of magnitude lower than the average luminosity of known FRBs. The luminosity is compatible with that of bright Crab giant pulses reported by Bera & Chengalur (2019), although the pulse width is at least three orders of magnitude wider than the case of the Crab giant pulse. The luminosity is also similar to the case of SGR J1935+2145 ($\sim 7 \times 10^{36} \text{ erg/s}$ CHIME/FRB Collaboration et al. 2020; Bochenek et al. 2020), although the pulse width is about 20 times larger than that of SGR J1935+2145 (i.e. 0.5 ms CHIME/FRB Collaboration et al. 2020). If the burst is real, and it is located in M82, it is compatible to the picture that a bright radio burst comes from a magnetar in the M82.

The measured DM ($1523 \text{ cm}^{-3} \text{ pc}$) of the candidate is compatible with both of the two scenarios, 1) a giant pulse from M82, and 2) an FRB at a cosmological distance. The DM contribution from the intergalactic medium between Milky Way and M82 ($\sim 1 \text{ cm}^{-3} \text{ pc}$, Prochaska & Zheng 2019) is negligible comparing to other contributions, i.e. Galactic foreground of $33 \text{ cm}^{-3} \text{ pc}$ (Yao et al. 2017), halo of local group $\sim 100 \text{ cm}^{-3} \text{ pc}$ (Prochaska & Zheng 2019). Thus, the major DM contribution ($1400 \text{ cm}^{-3} \text{ pc}$) results from M82, if M82 association is assumed. As shown by Westmoquette et al. (2007) and Heckman et al. (1990), the electron density in M82 increase from 100 cm^{-3} at 1-3 kpc outskirt to 1000 cm^{-3} around the galaxy nucleus. Therefore, the measured DM is compatible with M82 properties in the picture of an M82 hosted source. The other picture, i.e. a cosmological FRB is also possible. If the source is at a further cosmological distance, the source can be much more luminous. Using the model of Luo et al. (2018), the redshift will be $z = 1.3^{+0.03}_{-0.5}$

and the inferred isotropic peak luminosity is $1.9^{+0.1}_{-1.3} \times 10^{43} \text{ erg/s}$, which is compatible to the properties of the known FRB population (Luo et al. 2018). At this stage, we are lack of further detection, we can not conclude yet on the nature of the source, as both the M82 and the cosmological interpretation are possible.

In both of the two pictures, there is an event rate issue. If the burst is harbored by M82, the *inferred* event rate is $1/55 \approx 0.02 \text{ hour}^{-1}$. Considering the rareness of radio burst from the Galactic magnetar SGR J1935+2145 and the fact that M82 are smaller in stellar number comparing to the Milky Way, the inferred event rate value seems to be too high. If the burst is cosmological, we would expect to detect $10^{-2} \sim 10^{-3}$ FRB per day with NS26m (Luo et al. 2020a), which is still much lower than our inferred event rate. However, the star formation rate in M82 is a few times higher than that in the Milky Way (Kennicutt & Evans 2012), which may indicate that the event rate of radio burst phenomenon may correlate with the star formation rate. If so, we would expect more radio bursts can be found by monitoring those star burst galaxies.

ACKNOWLEDGEMENTS

The work is supported by CAS XDB23010200, Max-Planck Partner Group, National SKA program of China 2020SKA0120100, NSFC 11690024, CAS Cultivation Project for FAST Scientific. We also thank active players of the mobile game *Lighthouse Project* to help perform the candidate inspection, including Y. Zou, H. Y. Lin, J. Q. Li, J. Y. Li, Y. X. Jiang, etc.

DATA AVAILABILITY STATEMENT

The data underlying this article are available in a repository and can be accessed via https://github.com/zhanyige/M82_FRB_couloured_noise/blob/data/original_data.zip

REFERENCES

- Agarwal D., Aggarwal K., Burke-Spolaor S., Lorimer D. R., Garver-Daniels N., 2020, *MNRAS*, **497**, 1661
- Bera A., Chengalur J. N., 2019, *MNRAS*, **490**, L12
- Bochenek C. D., Ravi V., Belov K. V., Hallinan G., Kocz J., Kulkarni S. R., McKenna D. L., 2020, *Nature*, **587**, 59
- Bonetti L., Ellis J., Mavromatos N. E., Sakharov A. S., Sarkisyan-Grinbaum E. K., Spallicci A. D. A. M., 2016, *Physics Letters B*, **757**, 548
- Bonetti L., Ellis J., Mavromatos N. E., Sakharov A. S., Sarkisyan-Grinbaum E. K., Spallicci A. D. A. M., 2017, *Physics Letters B*, **768**, 326
- Burke-Spolaor S., Bailes M., Ekers R., Macquart J.-P., Crawford Fronefield I., 2011, *ApJ*, **727**, 18
- CHIME/FRB Collaboration et al., 2019a, *Nature*, **566**, 235
- CHIME/FRB Collaboration et al., 2019b, *ApJ*, **885**, L24
- CHIME/FRB Collaboration et al., 2020, *Nature*, **587**, 54
- Cordes J. M., McLaughlin M. A., 2003, *ApJ*, **596**, 1142
- Dewey R. J., 1994, *AJ*, **108**, 337
- Gallego J. D., López-Fernández I., Diez C., Barcia A., 2004, in Danneville F., Bonani F., Deen M. J., Levinstein M. E., eds, Society of Photo-Optical Instrumentation Engineers (SPIE) Conference Series Vol. 5470, Noise in Devices and Circuits II, pp 402–413, doi:10.1117/12.547097
- Gwinn C. R., Johnson M. D., 2011, *ApJ*, **733**, 51
- Hao L.-F., Wang M., Yang J., 2010, *Research in Astronomy and Astrophysics*, **10**, 805
- Harris F. J., 1978, *IEEE Proceedings*, **66**, 51
- Heckman T. M., Armus L., Miley G. K., et al., 1990, *Astrophysical Journal Supplement Series*, **74**, 833

⁵ <https://ned.ipac.caltech.edu>

- Jarrett T., Chester T., Cutri R., Schneider S., Huchra J., 2003, *The Astrophysical Journal*, 125, 525
- Kennicutt R. C., Evans N. J., 2012, *ARA&A*, 50, 531
- Kumar P., et al., 2019, *ApJ*, 887, L30
- Lee K. J., Bassa C. G., Janssen G. H., Karuppusamy R., Kramer M., Smits R., Stappers B. W., 2012, *MNRAS*, 423, 2642
- Lin L., et al., 2020, *Nature*, 587, 63
- Lorimer D. R., Bailes M., McLaughlin M. A., Narkevic D. J., Crawford F., 2007, *Science*, 318, 777
- Luo R., Lee K., Lorimer D. R., Zhang B., 2018, *Monthly Notices of the Royal Astronomical Society*, 481, 2320
- Luo R., Men Y., Lee K., Wang W., Lorimer D., Zhang B., 2020a, *Monthly Notices of the Royal Astronomical Society*
- Luo J., et al., 2020b, arXiv e-prints, [p. arXiv:2003.08586](https://arxiv.org/abs/2003.08586)
- Luo R., et al., 2020c, *Nature*, 586, 693
- Macquart J. P., et al., 2020, *Nature*, 581, 391
- Masui K. W., Sigurdson K., 2015, *Physical Review Letters*, 115, 121301
- McQuinn M., 2014, *ApJ*, 780, L33
- Men Y. P., et al., 2019, *mnras*, 488, 3957
- Petroff E., et al., 2016, *Publ. Astron. Soc. Australia*, 33, e045
- Press W. H., 1978, *Comments on Astrophysics*, 7, 103
- Prochaska J. X., Zheng Y., 2019, *Monthly Notices of the Royal Astronomical Society*, 485, 648
- Shao L., Zhang B., 2017, *Phys. Rev. D*, 95, 123010
- Spitler L. G., et al., 2016, *Nature*, 531, 202
- Tingay S. J., Kaplan D. L., 2016, *ApJ*, 820, L31
- Vafnsteín L., Zúbakov V., 1970, *Extraction of Signals from Noise*. Dover books on physics and mathematical physics, Dover Publ., Incorporated, <https://books.google.co.kr/books?id=E2ksAAAAYAAJ>
- Van der Vaart A. W., 2000, *Asymptotic statistics*. Cambridge Series in Statistical and Probabilistic Mathematics Vol. 3, Cambridge university press
- Wang N., Manchester R. N., Zhang J., Wu X., Yusup A., Lyne A., Cheng K., Chen M., 2001, *Monthly Notices of the Royal Astronomical Society*, 328, 855
- Wei J.-J., Gao H., Wu X.-F., Mészáros P., 2015, *Physical Review Letters*, 115, 261101
- Westmoquette M., Smith L., Gallagher III J., O'Connell R., Rosario D., De Grijs R., 2007, *The Astrophysical Journal*, 671, 358
- Wu X.-F., et al., 2016, *ApJ*, 822, L15
- Yao J., Manchester R., Wang N., 2017, *The Astrophysical Journal*, 835, 29
- Zhang S.-N., 2016, preprint, ([arXiv:1601.04558](https://arxiv.org/abs/1601.04558))
- Zhang Y. G., Gajjar V., Foster G., Siemion A., Cordes J., Law C., Wang Y., 2018, *ApJ*, 866, 149
- Zhang C., et al., 2020, *A&A*, 642, A26
- Zhou B., Li X., Wang T., Fan Y.-Z., Wei D.-M., 2014, *Phys. Rev. D*, 89, 107303

APPENDIX A: STATISTICAL PROPERTIES OF S WITH COLOURED NOISE

We denote the coloured noise component as r_i , and white noise component as n_i with index i indicating the temporal sampling. The de-dispersed one dimensional time series is $s_i = r_i + n_i$. The summation of s_i , i.e. $u \equiv \sum_{|t-t_0|<w} s_i$, follows Gaussian distribution, because a linear superposition of Gaussian variable is still Gaussian. In this way, the detection statistic, being a square of Gaussian ($S \propto u^2$), must follow a one dimensional scaled χ^2 distribution.

We can compute the mean and standard deviation to fully determine the distribution. By expanding the correlation, one can

show that

$$\langle S \rangle = 1 + \frac{1}{N_{\text{box}}} \sum_{i,j} \gamma_{ij}, \quad (\text{A1})$$

$$\langle S^2 \rangle - \langle S \rangle^2 = 2 \left(1 + \frac{1}{N_{\text{box}}} \sum_{i,j} \gamma_{ij} \right)^2. \quad (\text{A2})$$

Here $\langle \cdot \rangle$ indicates the ensemble average. $\gamma_{i,j}$ is the two-point correlation of coloured noise normalised by the total noise RMS, i.e.

$$\gamma_{ij} = \frac{\langle r_i r_j \rangle}{\sigma^2 + \sigma_r^2}. \quad (\text{A3})$$

σ_r is the RMS of the coloured noise. The summation of index i and j runs within the pulse duration, which includes N_{box} data points. The distribution of the S with coloured noise is thus

$$f(S|N_{\text{box}}) = \frac{1}{\sqrt{2\pi}} \left(\frac{S}{\langle S \rangle} \right)^{-\frac{1}{2}} e^{-\frac{S}{2\langle S \rangle}}. \quad (\text{A4})$$

Note here that the distribution function $f(S|N_{\text{box}})$ depends on the pulse width, since it depends on N_{box} . The term $\sum_{i,j} \gamma_{ij}$ can be simplified with the help of coloured noise power spectrum density ($S(f)$), which is a Fourier transform of the two point correlation function. By definition, we have

$$\gamma_{i,j} = \frac{1}{\sigma^2 + \sigma_r^2} \int_0^\infty S(f) e^{2\pi i f (t_i - t_j)} df, \quad (\text{A5})$$

and, after interchanging the order of summation and integration, one gets

$$\sum_{i,j} \gamma_{i,j} = \frac{1}{\sigma^2 + \sigma_r^2} \int_0^\infty S(f) \frac{\sin^2(f N_{\text{box}} \pi \Delta T)}{\sin^2(f \pi \Delta T)} df, \quad (\text{A6})$$

with ΔT being the sampling time. The above equation can be further simplified, if we replace the discrete summation using the integral, i.e. assuming $\sum_i \approx \frac{N}{T} \int_0^T dt$, we have

$$\sum_{i,j} \gamma_{i,j} = \frac{1}{\sigma^2 + \sigma_r^2} \int_0^\infty S(f) \frac{\sin^2(f N_{\text{box}} \pi \Delta T)}{(f \pi \Delta T)^2} df, \quad (\text{A7})$$

There are two major types of correlated noise, 1) the red noise dominated by low frequency components and 2) quasi-monochromatic noise dominated by a single frequency component.

For case 1), we can assume that the noise spectrum is a power-law function, i.e. $S(f) = A f^{-\alpha}$, where α is the spectral index. one gets (similar computation can be found in Lee et al. (2012)),

$$\begin{aligned} \sum_{i,j} \gamma_{i,j} &= N_{\text{box}}^2 \frac{\sigma_r^2}{\sigma^2 + \sigma_r^2} \frac{\alpha - 1}{\pi} \times \\ &\left[(2\pi)^\alpha \Gamma(-1 - \alpha) \sin\left(\frac{\pi\alpha}{2}\right) + \right. \\ &\left. \frac{2\pi}{\alpha^2 - 1} {}_1F_2\left(\frac{1-\alpha}{2}; \frac{3}{2}, \frac{3-\alpha}{2}, -\pi^2\right) \right]. \quad (\text{A8}) \end{aligned}$$

Here Γ is the gamma function, and ${}_1F_2$ is the hypergeometric function. For spectral index runs within $\alpha \in [1, 10]$, the above result can be approximated by the average value

$$\sum_{i,j} \gamma_{i,j,\text{power}} \approx \frac{N_{\text{box}}^2}{100} \frac{\sigma_r^2}{\sigma^2 + \sigma_r^2}, \quad (\text{A9})$$

which leads to equation (4) with $\kappa \approx 1/100$. For the quasi-monochromatic case, the spectral density is approximated by the

Dirac's δ function, and one has

$$\sum_{ij} \gamma_{i,j,\text{mono}} = N_{\text{box}}^2 \frac{\sigma_r^2}{\sigma^2 + \sigma_r^2} \text{sinc}^2(\pi f_0 T), \quad (\text{A10})$$

with f_0 being the frequency of monochromatic noise. For $fT \ll 1$, we have $\sum_{ij} \gamma_{i,j,\text{mono}} = N_{\text{box}}^2 \sigma_r^2 / (\sigma^2 + \sigma_r^2)$, i.e. $\kappa = \text{sinc}^2(\pi f_0 T)$.

For most of the FRB searches, one will only record the signal above certain threshold, saying $S \geq S_0$. In order to compare the observation, we compute here the expectation and standard deviation of S with threshold selection $S \geq S_0$. From the distribution function, we have

$$\langle S \rangle|_{S \geq S_0} = \frac{\int_{S_0}^{\infty} f(S) S ds}{\int_{S_0}^{\infty} f(S) ds}, \quad (\text{A11})$$

$$\langle S^2 \rangle|_{S \geq S_0} = \frac{\int_{S_0}^{\infty} f(S) S^2 ds}{\int_{S_0}^{\infty} f(S) ds}, \quad (\text{A12})$$

which produce

$$\langle S \rangle|_{S \geq S_0} = \frac{\langle S \rangle \text{erfc}\left(\sqrt{\frac{S_0}{2\langle S \rangle}}\right) + \sqrt{\frac{2S_0\langle S \rangle}{\pi}} e^{-\frac{S_0}{2\langle S \rangle}}}{\text{erfc}\left(\sqrt{\frac{S_0}{2\langle S \rangle}}\right)}, \quad (\text{A13})$$

$$\langle S^2 \rangle|_{S \geq S_0} = \frac{3\langle S \rangle^2 \text{erfc}\left(\sqrt{\frac{S_0}{2\langle S \rangle}}\right) + \sqrt{\frac{2S_0\langle S \rangle}{\pi}} (S_0 + 3\langle S \rangle) e^{-\frac{S_0}{2\langle S \rangle}}}{\text{erfc}\left(\sqrt{\frac{S_0}{2\langle S \rangle}}\right)} \quad (\text{A14})$$

If one is interested in the distribution of S for all pulses found in the given data (denoted as $\mathcal{F}(s)$). We can sum over the possible choice of N_{box} . The number of independent pulse sample for the given data is $T/(\Delta T N_{\text{box}})$, and the distribution of S for all *observed* pulses is given by

$$\mathcal{F}(s) \propto \sum_{N_{\text{box}}} f(S|N_{\text{box}}) \frac{T}{\Delta T N_{\text{box}}} \quad (\text{A15})$$

This paper has been typeset from a \LaTeX file prepared by the author.

APPENDIX B: BEAR DETECTION PLOT

In this section, we show the BEAR candidate sifting plot for the signal we found, i.e. Figure B1. As one can see from sub-panel j), the signal is contributed from channels across rather wide bandwidth. Sub-panel h) shows that the burst can not be found in the zero-dm time series, which verify the dispersive nature of the burst, and sub-panel g) further indicates that the DM index is around -2.

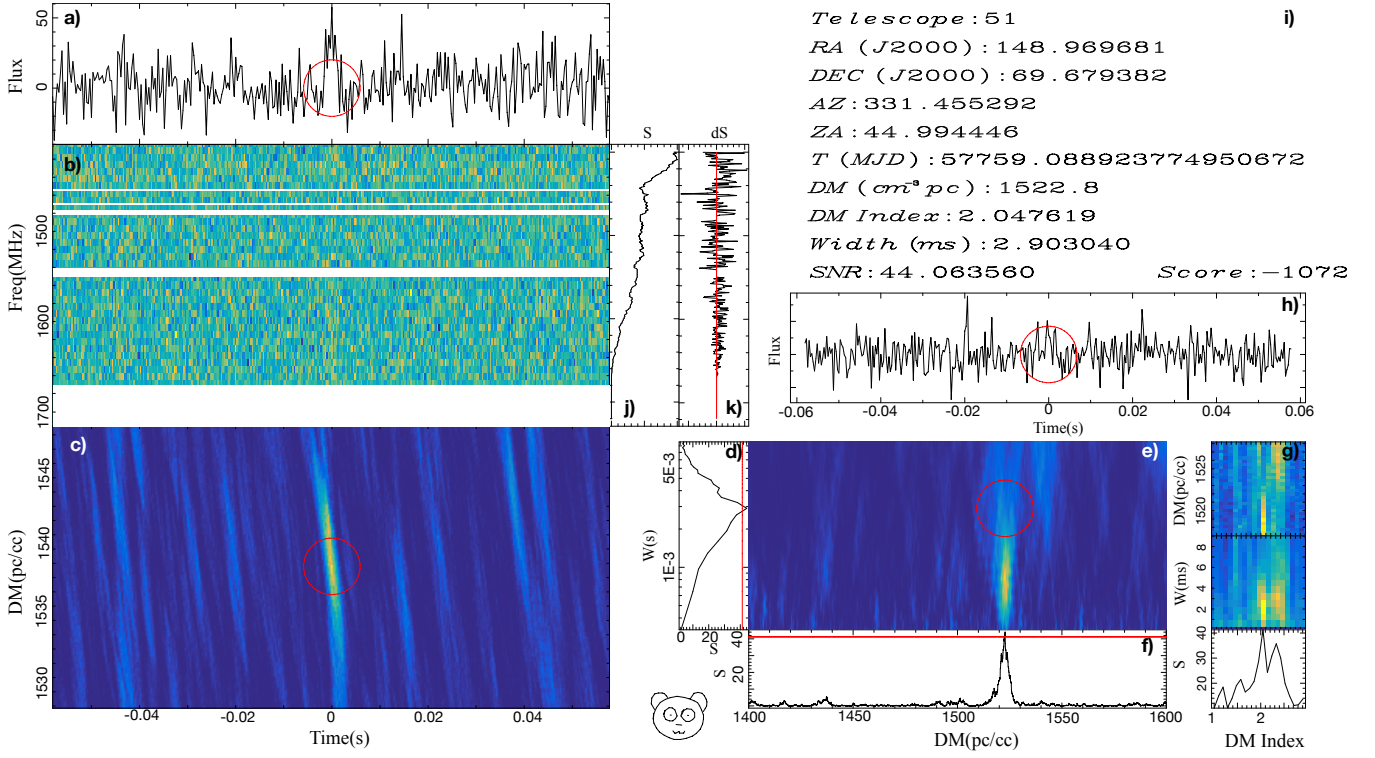


Figure B1. A FRB candidate found along the M82 direction. The plot is produced by BEAR. a) the de-dispersed candidate pulse profile with a red circle indicating the pulse time of arrival, b) the dynamical spectrum after de-dispersion, c) the likelihood ratio test statistics S as a function of DM and time, d) S as a function of pulse width, e) S as a function of DM (x-axis) and pulse width (y-axis), red circle label the best estimated DM value, f) S as a function of DM, where red horizontal lines indicates false alarm rate of 10^{-10} , g) DM, pulse width and S as a function of DM index, h) the time series de-dispersed at 0 DM, i) the basic information of the pulse, j) the integration of S (x-axis) changes over frequency channel, k) the contribution of S from each frequency channel.